A study of the effect of the synthesis conditions of titanium dioxide on its morphology and cell toxicity properties

Kh. Pourghorbani dinachali [a], M.R. Fadavieslam [a],[*], S. Zavareh [b]

[a] School of Physics, Damghan University, Damghan, Iran
[b] School of Biology, Damghan University, Damghan, Iran

Abstract   In this study, titanium dioxide nanoparticles (NPs) were synthesized using the home microwave method, and the effect of the microwave irradiation time on the structure of NPs was investigated. In addition, the morphological effect of these NPs on the toxicity of HDMSCs cells was investigated. The crystalline structure and morphology of the NPs were analyzed using X-ray diffraction (XRD), Fourier transform infrared spectroscopy (FTIR), and field emission scanning electron microscopy (FE-SEM); the cytotoxicity was determined by the methyl thiazolyl tetrazolium (MTT) assay. X-ray diffraction analysis revealed that all thin films had a polycrystalline nature with an anatase phase of TiO_2. It was also found that the crystallite size increased with increasing microwave radiation time. The FTIR spectrum showed Ti-O-Ti properties by the peak in the range between 527 and 580 cm^{-1}. Further, the FE-SEM images showed that the grain size increased with increasing irradiation time. The MTT assay results showed that the accumulation of NPs leads to toxicity.

1. Introduction

The significant interest in the research and development of nanomaterials, especially NPs, is due to their attractive properties, which are evident in their small size, remarkably high surface area activity, and excellent catalytic, optical, and electrical properties (Azim et al., 2015). Among various nanomaterials, titanium dioxide (TiO_2) NPs occupy a special position due to their high availability, high photocatalytic activity, high thermal stability, and low price, making them useful for the production of paints, plastics, paper, cosmetics, medicine, food, furniture, etc. (Ahmad et al., 2020, Kurban et al., 2020, Mancuso et al., 2020, Safiay et al., 2021, Subagyo et al., 2022). Some methods for the synthesis of titanium dioxide NPs include sol–gel (Muthee and Dejene 2021), solvothermal (Dubey et al., 2020), Hydrothermal (Santhi et al., 2020), and microwave (Falk et al., 2018). The microwave method, which includes both industrial and household microwaves, is a practical option to significantly reduce the synthesis time. With this method, rapid and high-quality synthesis

can be achieved. In this method, the sample is directly heated by microwaves and has a shorter heat transfer time than conventional heating (Horikoshi and Serpone).

Titanium dioxide occurs naturally in polymorphic crystalline forms, such as stable rutile, brookite, and anatase, synthesized in the laboratory. Anatase is a low-temperature and chemically stable phase, while rutile is a thermodynamically essential form of titanium dioxide. Anatase can be converted to rutile at higher temperatures by phase transformation. This conversion of anatase to rutile occurs at high temperatures above 400 °C. However, with optimized synthesis parameters, this phase transformation can also occur at room temperature (Madhusudan Reddy et al., 2003, Ayyaz et al., 2020).

Titanium dioxide is a food additive with no nutritional value. It is commonly used in processed foods to provide a whitening effect. Concern about the use of NPs in food has recently been increasing, and studies on the determination and quantification of food-grade TiO_2 in commercial foods have risen with it (Hwang et al., 2019).

The special properties of NPs, such as small size, high number per given mass, and large specific surface area, have raised worldwide concern about their fate in biological systems. Moreover, NPs can accumulate in the liver, kidney, spleen, lung, heart, and brain and cause various inflammatory responses (Azim et al., 2015). For example, titanium dioxide caused cytotoxicity in pulmonary alveolar macrophages. In addition, a correlation between particle size and lung injury has been found (Liu et al., 2013). Although the bulk form of titanium dioxide is biologically inert, the nano-sized forms exhibit interesting physical, chemical, and biological properties related to size. For example, NPs with a diameter of $\leq$ 30 nm undergo drastic changes that increase their interfacial reactivity and modulate toxicological properties (Demir et al., 2015). Despite the crystallinity of TiO_2 NPs, their genotoxicity mainly depends on their particle size. Smaller titanium dioxide NPs have a stronger genotoxic effect than larger ones because they easily penetrate the nucleus and cytoplasm of the cell. Larger agglomerations of titanium dioxide NPs cause DNA damage (Rashid et al., 2021). The special properties of NPs, such as small size, high number per given mass, and large specific surface area, have raised worldwide concern about their fate in biological systems. Moreover, NPs can accumulate in the liver, kidney, spleen, lung, heart, and brain and cause various inflammatory responses (Azim et al., 2015). For example, titanium dioxide caused cytotoxicity in pulmonary alveolar macrophages. In addition, a correlation between particle size and lung injury has been found (Liu et al., 2013). Although the bulk form of titanium dioxide is biologically inert, the nano-sized forms exhibit interesting physical, chemical, and biological properties related to size. For example, NPs with a diameter of $\leq$ 30 nm undergo drastic changes that increase their interfacial reactivity and modulate toxicological properties (Demir et al., 2015). Despite the crystallinity of TiO_2 NPs, their genotoxicity mainly depends on their particle size. Smaller titanium dioxide NPs have a stronger genotoxic effect than larger ones because they easily penetrate the nucleus and cytoplasm of the cell. Larger agglomerations of titanium dioxide NPs cause DNA damage (Rashid et al., 2021). Most toxicologists believe that NPs have higher toxicity due to their larger surface area, increased chemical reactivity, and easier cell penetration (Xie et al., 2015). Titanium dioxide NPs are currently one of the most widely used nanomaterials in everyday life, and their production and consumption are increasing worldwide. The use of these NPs makes it necessary that the toxic effects of these NPs on human health be studied.

In this study, TiO2 NPs were synthesized using the microwave method. Then, the effect of the irradiation time on the structure of the NPs was investigated. The toxicity of the synthesized NPs on bone marrow stem cells in an in vitro model was also investigated to determine the effect of the nanoparticle size on their toxicity.

2. Experimental procedures

To synthesize titanium dioxide NPs, 0.3 g of N-vinylpyrrolidone (PVP) was dissolved in 15 ml of dry ethanol. This solution was stirred at 30 °C for 30 min until a clear solution was obtained. In parallel, 3 ml of titanium isoproxide was added dropwise in 30 ml of absolute dry ethanol and then stirred at 30 °C for 15 min until a clear milky solution was obtained. Then the obtained PVP solution was slowly added to the titanium isoproxide solution. The finished solution was transferred to a Pyrex bottle and placed on the bottom of the microwave oven (input 300 W, 2.45 GHz, SAMSUNG brand). The sintering times were 3, 4, 2 + 2, 5, and 3 + 2 min and were designated F_1, F_2, F_3, F_4, and F_5, respectively. For the two-step irradiation times 2 + 2 and 2 + 3, the solutions were first irradiated in the microwave oven for 3 and 2 min, respectively, and then irradiated again for 2 min each after a 40-second break. The resulting suspension was centrifuged at 4000 rpm for 5 min to separate the liquid phase from the solid. After centrifugation, white precipitated solid particles were obtained. They were then placed in an oven at 90 °C for 24 h. Finally, the obtained powder was calcined at 500 °C for one hour to remove the residual organic reagents and to obtain the crystal structure of TiO_2. The structural properties were investigated by X-ray diffraction (XRD) using a D8 Advance Bruker X-ray diffractometer with Cu-Kα radiation (λ = 0.154056 nm) spectra in a 2θ range of 10°-80°. Surface morphology was studied by field emission scanning electron microscopy (FE-SEM; HITACHI S-4160). FTIR spectroscopy in the wavenumber range from 400 to 4000 cm^{-1} at room temperature using a VERTEX 80 V spectrometer.

Human-derived bone marrow mesenchymal stem cells (HDMSCs) were obtained from the Pasteur Institute cell bank in Iran. The cells were treated with antibiotics (penicillin 100 IU/mL, streptomycin 100 mg/mL). HDMSCs were maintained in an incubator at 37 °C and 5% CO_2. The culture cells with round spindle morphology observed (Fig. 1). For exposure studies, HDMSCs were cultured in 96-well dishes in DMEM supplemented with 10% FBS one day before exposure. For the exposure studies, the suspension of TiO_2 NPs
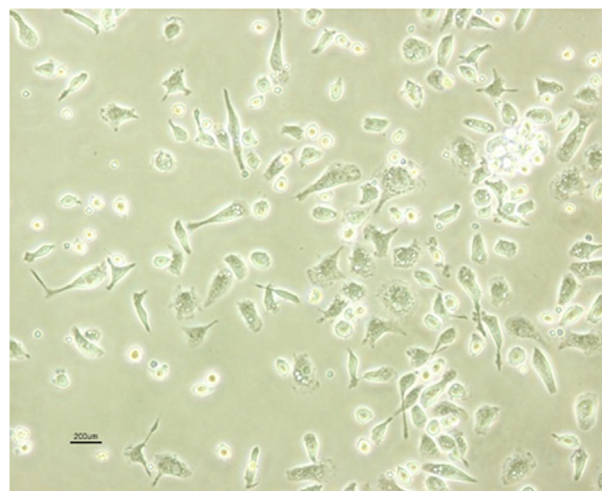

Fig. 1 morphology of Human bone marrow stem cells (HDMSCs).

was diluted in DMEM and added to the cells. For the control, the cell culture medium was diluted with water to ensure that the dilution of the medium by the aqueous TiO_2 NPs suspension did not affect the cell performance.

MTT assays were performed to measure cellular mitochondrial activity as previously described by Mosmann (1983) with some modifications. Briefly, the cells (1×10^4 /well) were incubated in DMEM in the presence or absence of TiO_2 NPs for 24 h at 37 °C and 5% CO_2. The test medium was then removed, and the cells were cultured in DMEM supplemented with 100 μl of MTT (0.5 $\frac{mg}{ml}$) for 1 h at 37 °C and 5% CO_2. The MTT solution was then removed, and DMSO was added to each well. The optical density (OD) was measured using an Eliza reader (Bio-Rad, Hercules, CA) at a wavelength of 570 nm (Rashid et al., 2021). The mean OD ratio of treatment wells to control wells was considered the cell survival rate for each treatment. The desired experimental concentrations were 3, 6, 12, 24 $\frac{\mu g}{ml}$, and the cells were exposed to TiO_2 NPs for 24 and 48 h. All experiments were performed in 4 replicates. All data were analyzed using IBM SPASS version 24. After testing the statistical distribution and confirming normality with the Shapiro's test, differences between groups were examined with the One-Way ANOVA and the TUKEY supplemental test. For all analyses, ($P < 0.05$) was considered statistically significant.

3. Results and discussions

3.1. Structural characterization

The XRD peaks provide information about crystallite size, structure, and lattice strain. Fig. 2 shows the XRD diffraction patterns of the TiO_2 samples. From the plots, the anatase phase was confirmed by peaks at $2\theta \approx 25.3°$, 37.8°, 48°, 54°, 55°, and 62.6°, corresponding to orientation planes (1 0 1), (0 0 4), (0 2 0), (0 1 5), (1 2 1), and (0 2 4), respectively. All the peaks observed in these spectra were in good agreement with the existing JCPDS data No. 21–1272 (Arabi et al., 2020). The highest intensity of the diffraction peak at $\sim 25.3°$, corresponding to plane (1 0 1), shows a oriented anatase polycrystal structure for all samples, consistent with previous reports of microwave synthesized TiO_2 (Mohadesi and Ranjbar 2016,
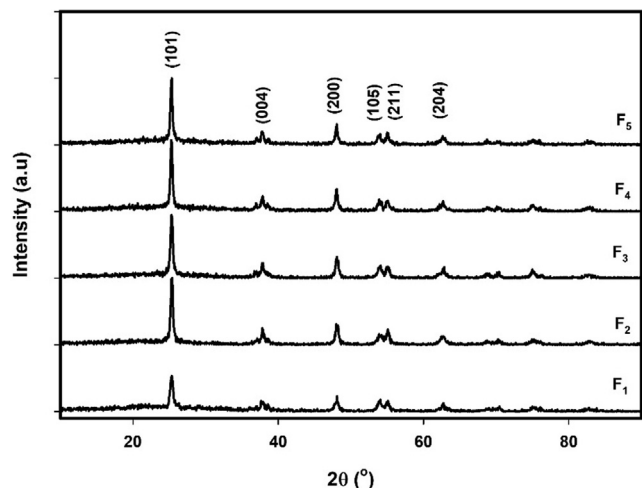

Fig. 2 XRD patterns of samples F1, F_2, F_3, F_4 and F_5.

Andrade-Guel et al., 2019, Ayyaz et al., 2020, Madurai Ramakrishnan et al., 2020).

The crystallite size (Ds) was estimated using the Scherrer formula (Ikram et al., 2020):

$$D_s = \frac{k\lambda}{\beta \cos \theta} \tag{1}$$

where k, called the shape factor, is a constant ($\sim$0.9) for spherical particles, λ represents the wavelength of the incident X-ray, β is the full width at half maximum, and θ defines the Bragg angle. Table 1 shows the results for the crystallite size (Ds). The crystallite size for plane (1 0 1) is larger for all samples, indicating that crystal growth was higher on this plane.

The average crystallite size of the samples was determined using the Halder-Wagner method, where the full width at half maximum of the physical profile can be written as follows:

$$\beta_{hkl}^2 = \beta_l \beta_{hkl} + \beta_G^2 \tag{2}$$

Where, β_l and β_G are the full width at half maximum of the Lorentzian and Gaussian functions.

This method gives more weight to the peaks in the lower and middle angular regions, where the overlap of the diffracting peaks is insignificant. The relation between the crystallite size and the lattice strain according to the Halder-Wagner method is given as follows (Rebhi et al., 2009):

$$\left(\frac{\beta_{hkl}^*}{d_{hkl}^*}\right)^2 = \frac{1}{D_{H-W}} \frac{\beta_{hkl}^*}{d_{hkl}^{*\,2}} + \left(\frac{\varepsilon}{2}\right)^2 \tag{3}$$

Where $\beta_{hkl}^* = \frac{\beta_{hkl} \cos \theta_{hkl}}{\lambda}$ and $d_{hkl}^* = \frac{2 \sin \theta}{\lambda}$. The plot of equation (3), with term $\left(\frac{\beta_{hkl}^*}{d_{hkl}^{*\,2}}\right)$ along X-axis and $\left(\frac{\beta_{hkl}^*}{d_{hkl}^*}\right)^2$ along the Y-axis for each peak of the XRD pattern is shown in Fig. 3. The slope of the plotted straight lines indicates the average crystallite size, while the intercept indicates the intrinsic strain of samples F_1, F_2, F_3, F_4, and F_5. The values of ε and D_{H-W} are detailed in Table 1.

Lattice constants (a and c) were calculated using the following equation (Mancuso et al., 2020):

$$\frac{1}{d_{(hkl)}^2} = \left(\frac{h^2 + k^2}{a^2}\right) + \frac{l^2}{c^2} \tag{4}$$

Table 1 shows the results of the lattice constants. These results agree well with the JCPDS map No. 21–1272. According to the results of Table 1. The average crystallite size and strain of the nanocrystals in the F_3 sample are larger than in the F_2 sample. They are also larger in the F5 sample than in the F4 sample. In the cases with continuous irradiation, the particles have more collisions due to the irradiation time, and these intense collisions cause more sub-grain boundaries; an increase in grain boundaries makes the average crystallite size smaller. In contrast, interruptions in radiation cause more crystal disturbances and defects, resulting in higher strain. Furthermore, when the irradiation time increases from 3 s (F_1) to 5 s (F_4), the average crystallite size increases, releasing additional strain. This leads to a lower strain.

The chemical composition of the synthesized NPs was analyzed by FTIR spectra in the range of 400–4000 cm^{-1} to determine the quality and chemical conformation of the TiO_2 NPs. Fig. 4 shows the FTIR spectra of the samples. In this range, no absorption peak of KBr is visible because the absorption coefficient of KBr is far below 400 cm^{-1}, so only a complete spec-

Table 1 The results of the XRD characterization of samples F_1, F_2, F_3, F_4, and F_5.

| Sample	(hkl)	2θ (°)	FWHM (°)	Ds (nm)	D_{H-W} (nm)	ε (×10⁻²)	a = b (Å)	c (Å)
F_1	(101)	25.31	0.45	18	22.51	1.15	3.7891	9.4322
	(004)	37.82	0.5	17				
	(020)	47.98	0.59	15				
	(015)	53.94	0.69	13				
	(121)	54.99	0.55	16				
	(024)	62.64	0.7	13				
F_2	(101)	25.32	0.33	25	19.89	1.28	3.7854	9.4624
	(004)	37.85	0.7	12				
	(020)	48.03	0.46	19				
	(015)	53.98	0.95	9				
	(121)	55.06	0.45	20				
	(024)	62.59	0.96	10				
F_3	(101)	25.3	0.34	24	26.84	1.44	3.8092	8.2184
	(004)	37.83	0.62	14				
	(020)	48.04	0.49	18				
	(015)	53.95	0.65	14				
	(121)	55.06	0.47	19				
	(024)	62.59	0.94	10				
F_4	(101)	25.34	0.32	25	27.29	1.12	3.7898	9.3433
	(004)	37.78	0.56	15				
	(020)	47.97	0.36	24				
	(015)	53.88	0.52	17				
	(121)	55	0.5	18				
	(024)	62.58	0.8	12				
F_5	(101)	25.27	0.31	26	42.12	1.38	3.7891	9.5399
	(004)	37.78	0.37	23				
	(020)	47.98	0.32	27				
	(015)	54.96	0.6	15				
	(121)	55.11	0.6	15				
	(024)	62.63	0.73	13				
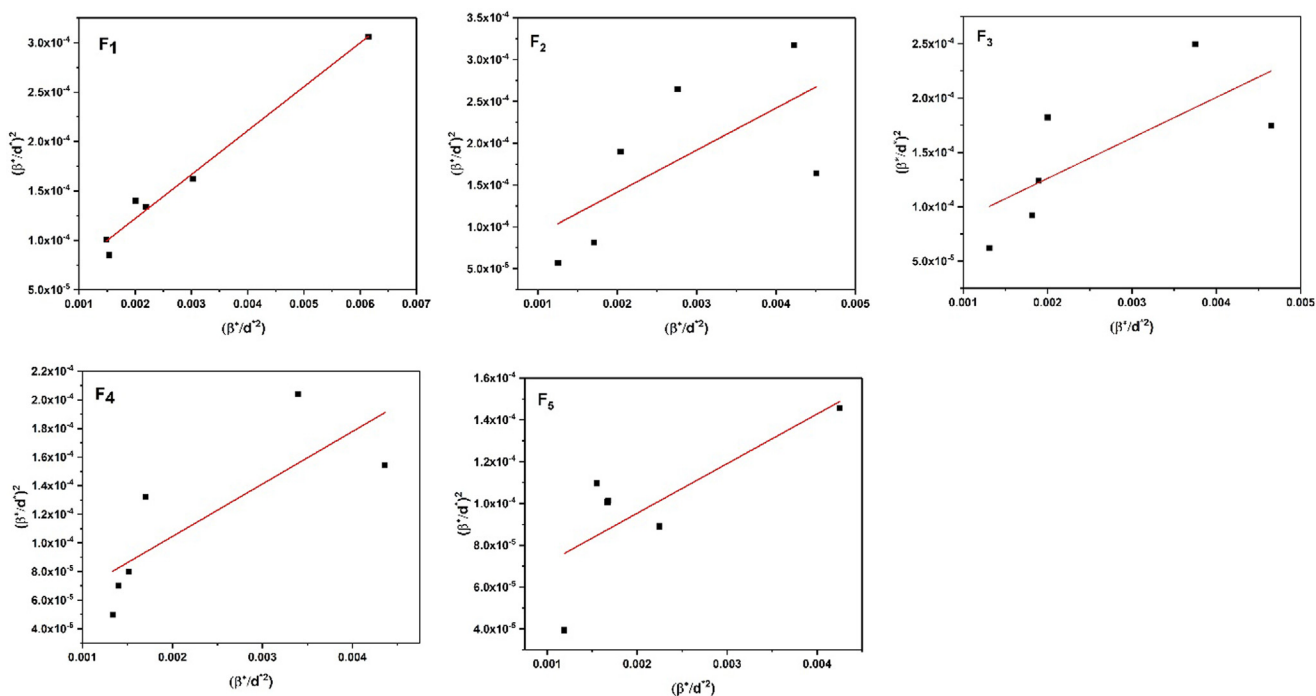
Fig. 3 Typical Williamson-Hall plots of samples F_1, F_2, F_3, F_4, and F_5.
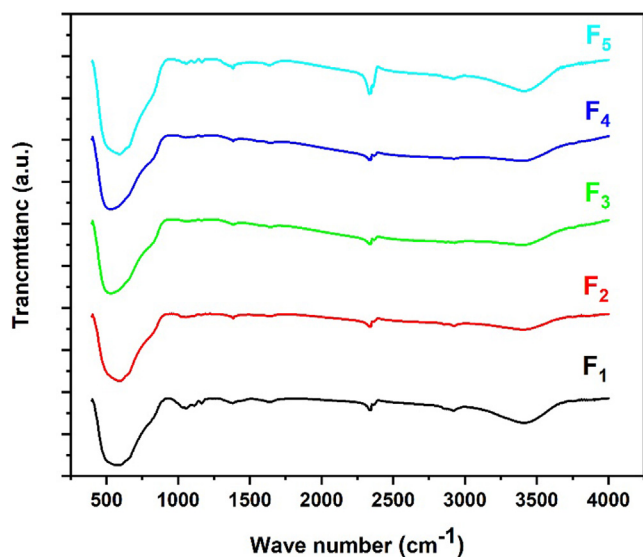
Fig. 4 FTIR patterns for samples F_1, F_2, F_3, F_4, and F_5.

Fig. 5 FE-SEM images for samples F_1, F_2, F_3, F_4, and F_5.

trum of the sample can be seen. The range from 527 to 580 cm^{-1} was used to observe the absorption band and associated bending vibrations of the TiO$_2$ lattice bond (O-Ti-O), which confirm the crystalline phase of TiO$_2$ (Lal et al., 2021). The weak band at 1381 cm^{-1} indicates C-H rock alkenes (Rajeswari et al., 2021). The peak at $\sim$ 1636 cm^{-1} corresponds to the stretching of titanium carboxylate due to titanium tetraisopropoxide and ethanol precursors (Rathore et al., 2020, Sharma et al., 2020). In addition, it could be due to the stretching and bending vibrations of the water molecule. The weak band at 2,920 cm^{-1} was attributed to the stretching vibration of C-H in the PVP molecular structure (Jang et al., 2016). The observed absorption peaks with a broad range from 3391 cm^{-1} to 3413 cm^{-1} are due to the interaction with the hydroxyl group (OH) of the water molecule (H2O) on the TiO$_2$ surface (Cheng et al., 2016, Dahham et al., 2020, Magdalane et al., 2021, Rajeswari et al., 2021). The peak at 3420 cm^{-1} corresponds to O-H stretching (Jang et al., 2016, Sagadevan et al., 2018). With increasing the duration of microwave irradiation, a shift of the peaks associated with the OH stretching to a higher wavelength is observed in the spectra.

Fig. 5 shows the FE-SEM images of the TiO$_2$ NPs of F_1, F_2, F_3, F_4, and F_5. It shows that the growth of agglomerates is almost spherical and has a uniform distribution. The size of NPs generally increases with irradiation time. The agglomerates of F_2 are about triple denser than F_1 because the irradiation time of sample F_2 is longer than that of sample F_1. When the irradiation process is interrupted, the material cools down, hindering the nucleation process and reducing the reaction rate. This results in the grain size of sample F_2 being larger than that of sample F_3. The irradiation times of samples F_4 and F_5 are the same, but the irradiation of sample F_4 is continuous, resulting in the grain size of sample F_4 being larger than that of sample F_5. The grain size of sample F_4 is larger than that of the others. This is because the irradiation time of this sample is longer and continuous. In our research, we found that the reaction time and pressure are crucial for the formation of TiO$_2$ NPs.
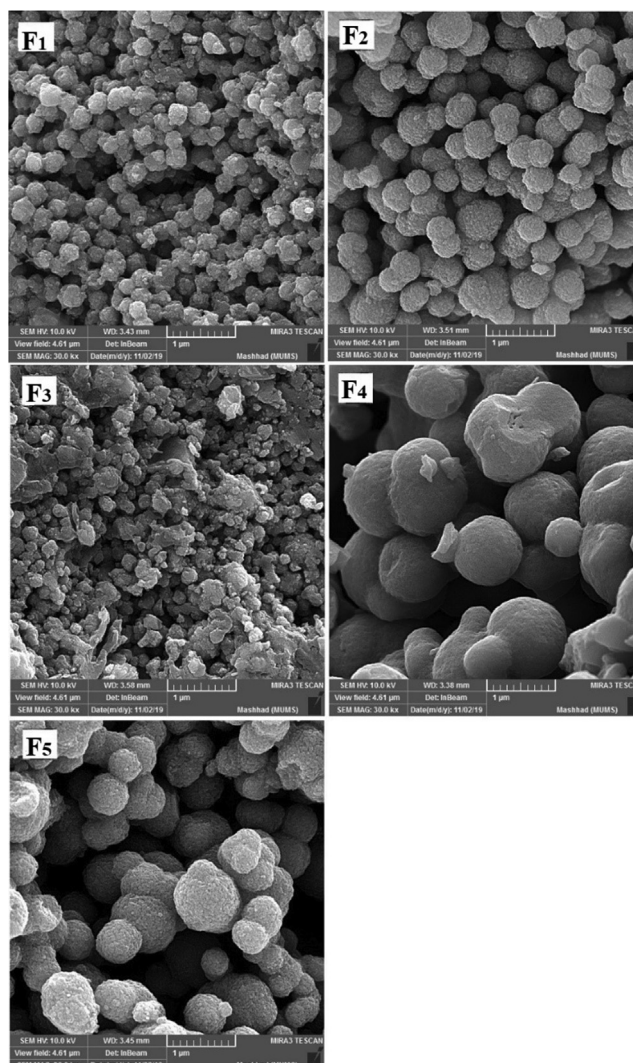
3.2. In vitro cytotoxicity of TiO$_2$ NPs

Before studying the toxicity of NPs, it is important to obtain information about the factors and properties that cause their toxicity. The physicochemical properties of NPs have an important influence on their toxicity. The results of other studies show that smaller NPs are more toxic than larger NPs [15, 34, 35]. This is because by reducing the size of nanoparticles, their cellular uptake occurs more easily and they can penetrate into the cell.

These studies show that the size of NPs contributes to their toxicity to living organisms. The size of NPs also affects their adsorption mechanism and storage capacity [36, 37]. Recent studies have not addressed the synthesis method and the evaluation of toxicity as a function of nanoparticle morphology [38–40].

The results of the MTT assay are shown in Figs. 6–13. Overall, the MTT assays showed a significant decrease in the viability of the cells in sample F_4. According to the results of FE-SEM for sample F_4, the agglomerates were fully compressed into a spherical shape, and this compression reduced
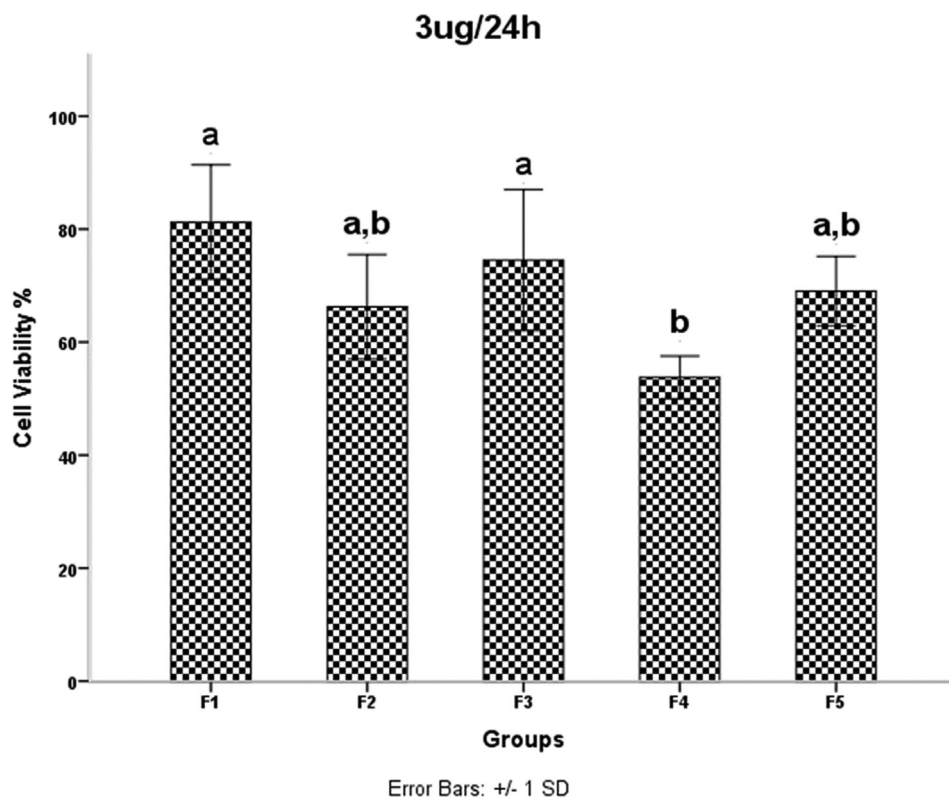
Fig. 6 HDMSCs were treated with a concentration of TiO_2 NPs 3 mgml for 24 h, then cell proliferation was assessed by the MTT assay. $P < 0.05$ was considered statistically significant.
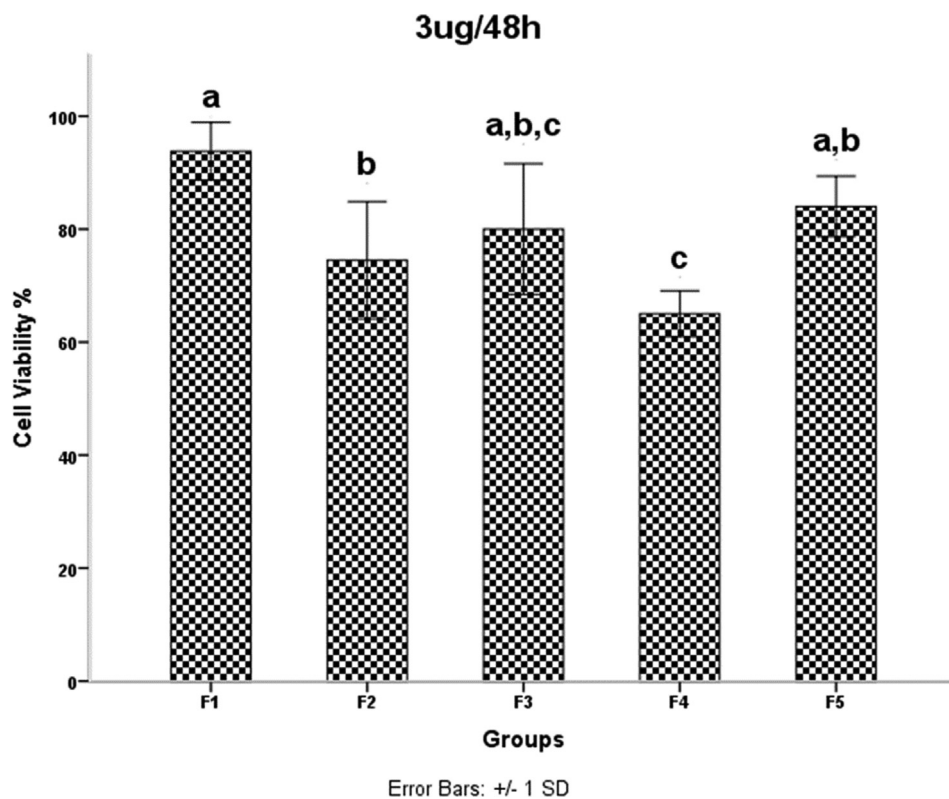

Fig. 7 HDMSCs were treated with a concentration of TiO_2 NPs 3 mgml for 48 h, then cell proliferation was assessed by the MTT assay. $P < 0.05$ was considered statistically significant.
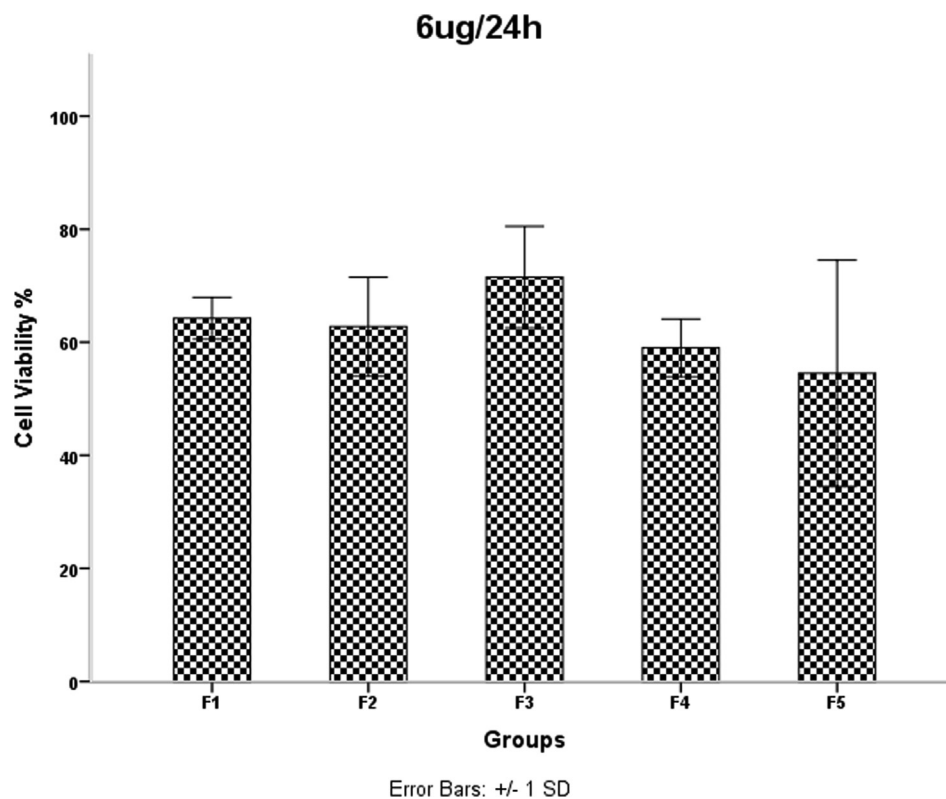
6ug/24h

Fig. 8 HDMSCs were treated with a concentration of TiO_2 NPs 6 mgml for 24 h, then cell proliferation was assessed by the MTT assay. $P < 0.05$ was considered statistically significant.

6ug/48h

Fig. 9 HDMSCs were treated with a concentration of TiO_2 NPs 6 mgml for 48 h, then cell proliferation was assessed by the MTT assay. $P < 0.05$ was considered statistically significant.
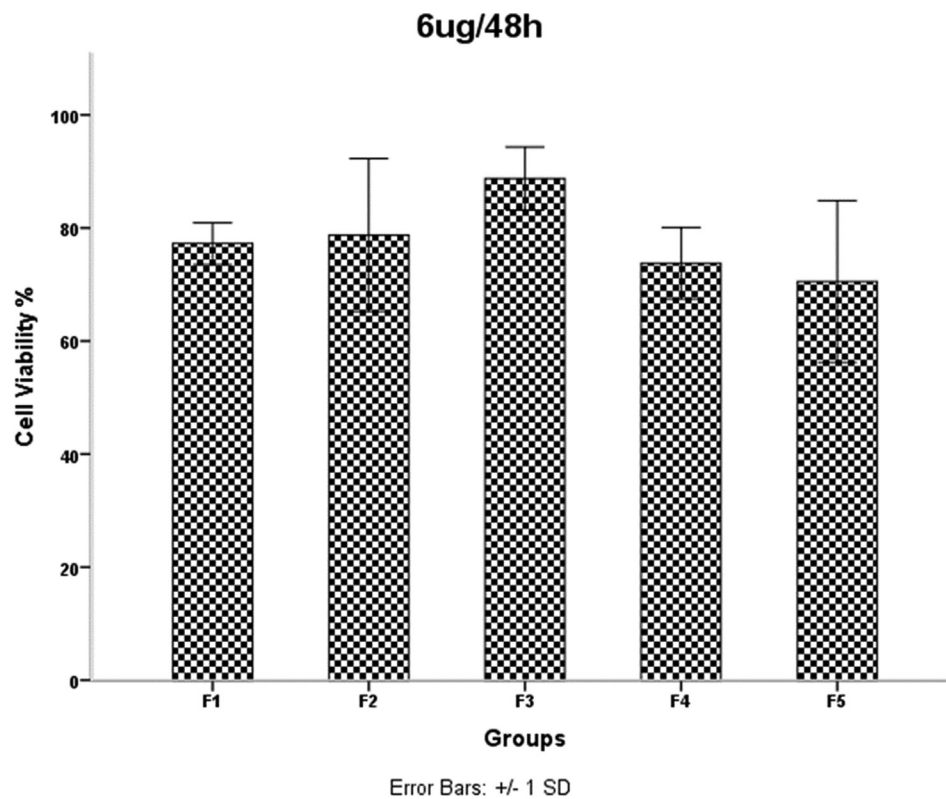
Fig. 10   HDMSCs were treated with a concentration of TiO$_2$ NPs of 12 mgml for 24 h, then cell proliferation was assessed by the MTT assay. P < 0.05 was considered statistically significant.

Fig. 11   HDMSCs were treated with a concentration of TiO$_2$ NPs 12 mgml for 48 h, then cell proliferation was assessed by the MTT assay. P < 0.05 was considered statistically significant.
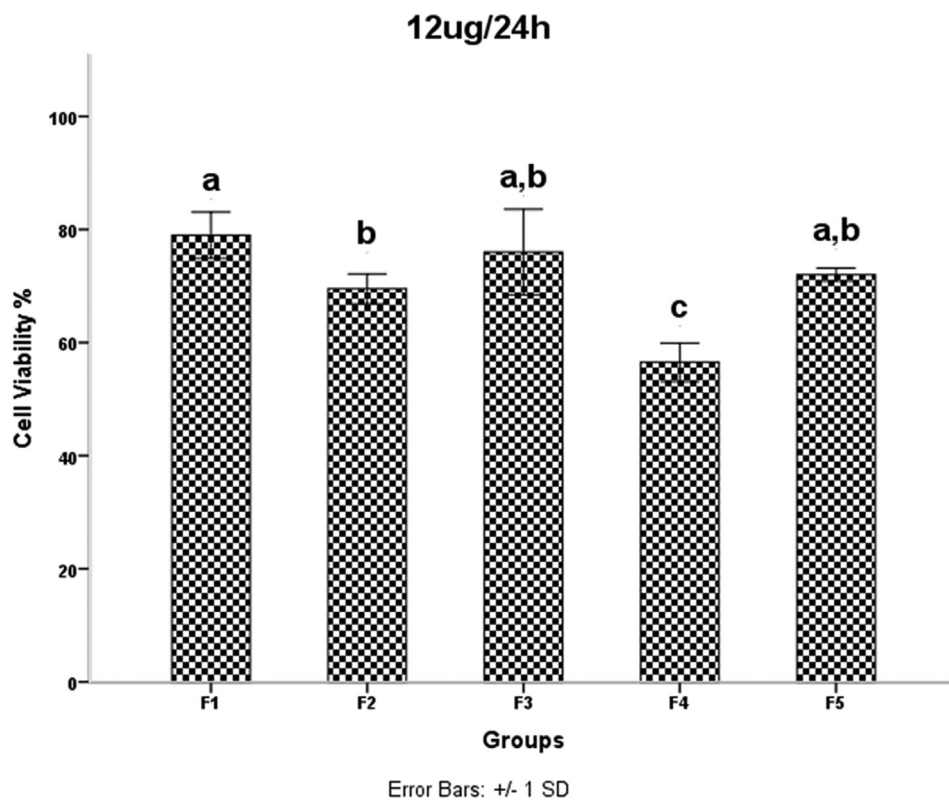
Fig. 12 HDMSCs were treated with a concentration of TiO$_2$ NPs 24 mgml for 24 h, then cell proliferation was assessed by the MTT assay. $P < 0.05$ was considered statistically significant.
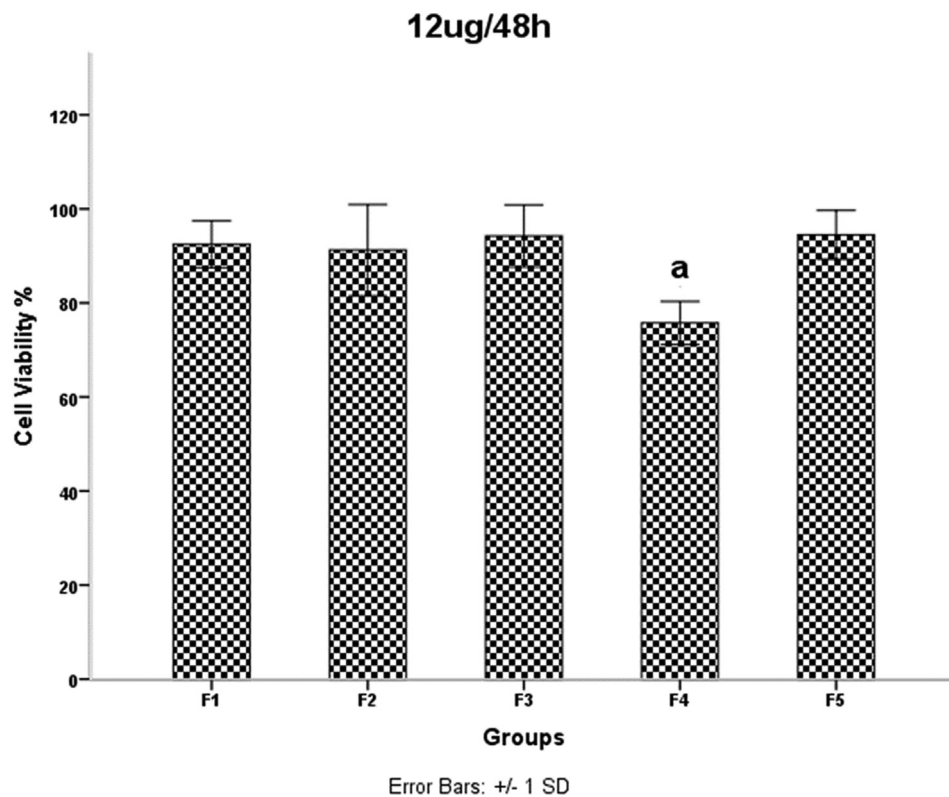

Fig. 13 HDMSCs were treated with a concentration of TiO$_2$ NPs 24 mgml for 48 h, then cell proliferation was assessed by the MTT assay. $P < 0.05$ was considered statistically significant.
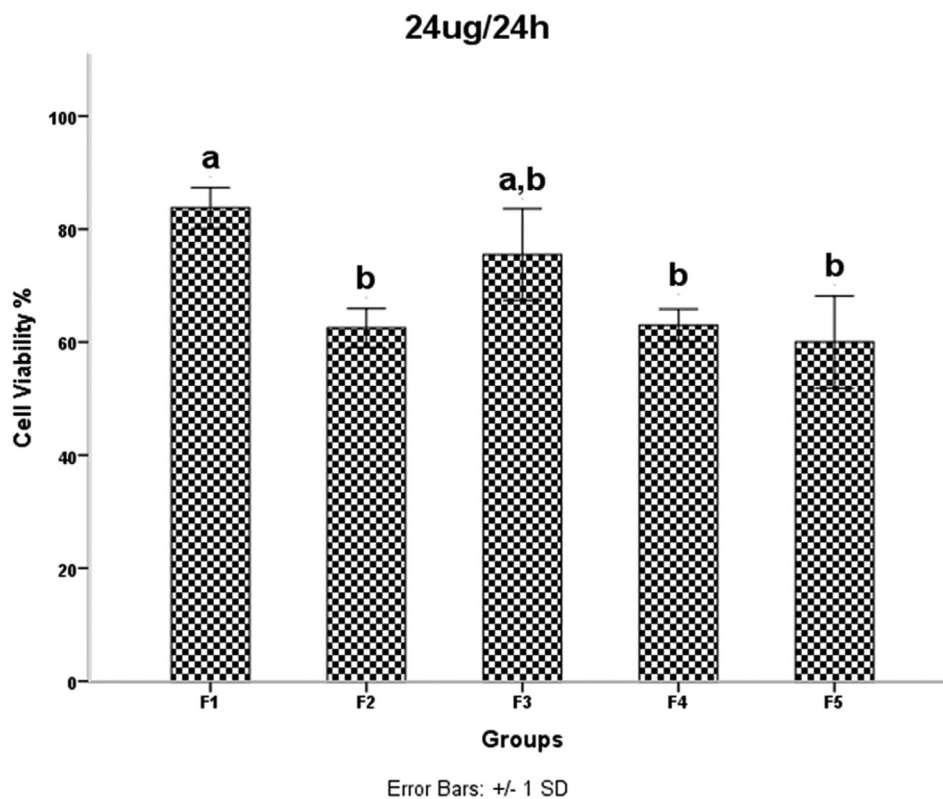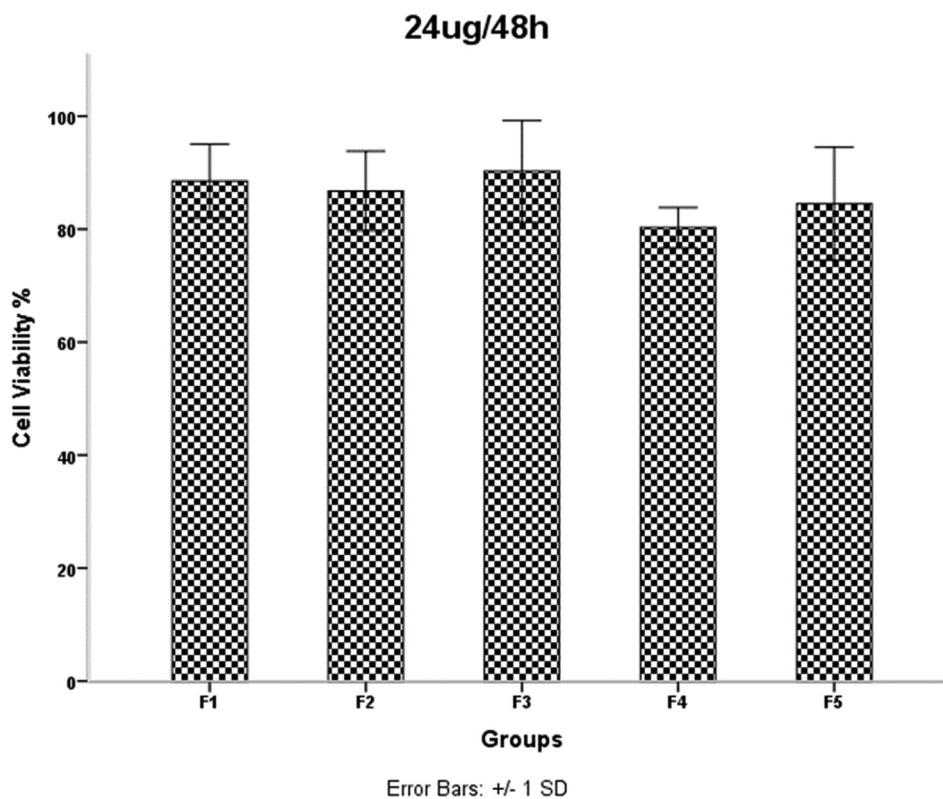
the subsidiary precincts, which in turn reduced the mobility and displacement of the NPs.

Examination of the results in Table 1 shows that increasing the irradiation time from 4 min (F_2) to 5 min (F_4) reduces the network strain. This decrease increases the density of agglomerates in the F_4 sample and results in decreased mobility and displacement of nanoparticles. The decreased mobility and displacement of nanoparticles increases cell killing and increases the toxicity of the F_4 sample. Although the average crystallite size is smaller in the F_2 sample than in the F_4 sample, the results of the MTT assay show that the percentage of cell viability is lower in the F4 sample. A 40-second pause in the F_5 synthesis process exerts pressure on and breaks the nanoparticle structure compared to F_4, resulting in increased strain and lattice failure. The increase in strain leads to the formation of subgrain boundaries and increases the irregularity of the agglomerates in sample F_5 compared to sample F_4. Therefore, according to the results of the MTT test, the survival rate of the cells in the F_4 sample is lower than the F_5 sample. It was shown that the accumulation of NPs leads to toxicity. In addition, cell viability was significantly higher in sample F_4 than in F_3. This is likely due to a 40-second pause in the irradiation time in the synthesis process, which affected the number of subsidiary precincts, leading to the high mobility of NPs. The same is true for NPs F_2 and F_3. The cell viability of sample F_3 was significantly higher than that of F_2. As the duration of the MTT assay increased, so did cell viability. The FE-SEM images show that the synthesis of NPs without a break during irradiation leads to increased compaction of the agglomerates. These agglomerates may reduce the mobility and inactivity of the NPs, leading to their accumulation and toxicity (Little et al., 2021). The toxicity evaluation in our study showed that the main cause of toxicity of these NPs was the compaction of the agglomerates, and the more compact the agglomerates were, the more toxicity the NPs showed (Kose et al., 2020). Although the dependence of toxicity on nanoparticle size has been reported, the MTT assay results of our samples for different concentrations and times showed no dependence of toxicity on crystallite or agglomerate size (Zhang et al., 2012).

4. Conclusions

In this work, we synthesized titanium dioxide NPs in a microwave oven and studied the toxicity of these particles. The results showed that at constant microwave oven power, the size of the crystals increases with increasing the duration of microwave irradiation. Moreover, a 40-s interruption of microwave irradiation during the synthesis of the nanoparticles leads to agglomerate densification. Furthermore, an increase in the microwave irradiation time also leads to the densification of the agglomerates. Therefore, the size and densification of NPs can be controlled during microwave synthesis. The MTT assay results showed no dependence of toxicity on crystallite size. On the toxicity of the NPs was found to depend on the densification of the agglomerates. Thus, a higher density of agglomerates leads to more toxicity.

References

Ahmad, I., Usman, M., Zhao, T.-K., et al, 2020. Bandgap engineering of TiO2 nanoparticles through MeV Cu ions irradiation. Arabian J. Chem. 13, 3344–3350. https://doi.org/10.1016/j.arabjc.2018.11.008.

Andrade-Guel, M., Díaz-Jiménez, L., Cortés-Hernández, D., et al, 2019. Microwave assisted sol–gel synthesis of titanium dioxide using hydrochloric and acetic acid as catalysts. Boletín de la Sociedad Española de Cerámica y Vidrio. 58, 171–177. https://doi.org/10.1016/j.bsecv.2018.10.005.

Arabi, N., Kianvash, A., Hajalilou, A., et al, 2020. A facile and green synthetic approach toward fabrication of Alcea- and Thyme-stabilized TiO2 nanoparticles for photocatalytic applications. Arabian J. Chem. 13, 2132–2141. https://doi.org/10.1016/j.arabjc.2018.03.014.

Ayyaz, M., Naz, M.Y., Shoukat, A., et al, 2020. Microwave plasma assisted sol-gel technique for synthesis of TiO2 nanoparticles. IOP Conf. Ser.: Mater. Sci. Eng. 863. https://doi.org/10.1088/1757-899x/863/1/012035.

Azim, S.A.A., Darwish, H.A., Rizk, M.Z., et al, 2015. Amelioration of titanium dioxide nanoparticles-induced liver injury in mice: Possible role of some antioxidants. Exp. Toxicol. Pathol. 67, 305–314. https://doi.org/10.1016/j.etp.2015.02.001.

Cheng, X., Yu, X., Xing, Z., et al, 2016. Synthesis and characterization of N-doped TiO2 and its enhanced visible-light photocatalytic activity. Arabian J. Chem. 9, S1706–S1711.

Dahham, O.S., Hamzah, R., Bakar, M.A., et al, 2020. Insight on the structural aspect of ENR-50/TiO2 hybrid in KOH/C3H8O medium revealed by NMR spectroscopy. Arabian J. Chem. 13, 2400–2413.

Demir, E., Akça, H., Turna, F., et al, 2015. Genotoxic and cell-transforming effects of titanium dioxide nanoparticles. Environ. Res. 136, 300–308. https://doi.org/10.1016/j.envres.2014.10.032.

Dubey, R.S., Pathan, H.M., Kale, B.B., et al, 2020. Solvothermal synthesis and characterisation of doped TiO₂ nanocrystals for light scattering applications. Journal. 15, 1120–1125.

Falk, G.S., Borlaf, M., López-Muñoz, M.J., et al, 2018. Microwave-assisted synthesis of TiO2 nanoparticles: photocatalytic activity of powders and thin films. J. Nanopart. Res. 20, 23. https://doi.org/10.1007/s11051-018-4140-7.

Hwang, J.-S., Yu, J., Kim, H.-M., et al, 2019. Food Additive Titanium Dioxide and Its Fate in Commercial Foods. Nanomaterials. 9, 1175.

Ikram, S., Jacob, J., Mehboob, K., et al, 2020. A novel approach to simultaneously enhance the Seebeck coefficient and electrical conductivity in rutile phase of TiO2 nanostructures. Arabian J. Chem. 13, 6724–6729. https://doi.org/10.1016/j.arabjc.2020.06.026.

Jang, I., Leong, H.J., Oh, S.-G., 2016. Effects of surfactants on the preparation of TiO2 nanoparticles in microwave-assisted sol-gel process and their photocatalytic activity. Korean J. Chem. Eng. 33, 1647–1652. https://doi.org/10.1007/s11814-016-0008-7.

Kose, O., Tomatis, M., Leclerc, L., et al, 2020. Impact of the Physicochemical Features of TiO2 Nanoparticles on Their In Vitro Toxicity. Chem. Res. Toxicol. 33, 2324–2337. https://doi.org/10.1021/acs.chemrestox.0c00106.

Kurban, H., Dalkilic, M., Temiz, S., et al, 2020. Tailoring the structural properties and electronic structure of anatase, brookite and rutile phase TiO2 nanoparticles: DFTB calculations. Comput. Mater. Sci. 183,. https://doi.org/10.1016/j.commatsci.2020.109843 109843.

Lal, M., Sharma, P., Ram, C., 2021. Calcination temperature effect on titanium oxide (TiO2) nanoparticles synthesis. Optik. 241,. https://doi.org/10.1016/j.ijleo.2021.166934 166934.

Little, S., Johnston, H.J., Stone, V., et al, 2021. Acute waterborne and chronic sediment toxicity of silver and titanium dioxide nanomaterials towards the oligochaete. Lumbriculus variegatus. NanoImpact. 21, 100291.

Liu, Y., Xu, Z., Li, X., 2013. Cytotoxicity of titanium dioxide nanoparticles in rat neuroglia cells. Brain Inj. 27, 934–939.

Madhusudan Reddy, K., Manorama, S.V., Ramachandra Reddy, A., 2003. Bandgap studies on anatase titanium dioxide nanoparticles. Mater. Chem. Phys. 78, 239–245. https://doi.org/10.1016/S0254-0584(02)00343-7.

Madurai Ramakrishnan, V., Pitchaiya, S., Muthukumarasamy, N., et al, 2020. Performance of TiO2 nanoparticles synthesized by

microwave and solvothermal methods as photoanode in dye-sensitized solar cells (DSSC). Int. J. Hydrogen Energy 45, 27036–27046. https://doi.org/10.1016/j.ijhydene.2020.07.018.

Magdalane, C.M., Priyadharsini, G.M.A., Kaviyarasu, K., et al, 2021. Synthesis and characterization of TiO2 doped cobalt ferrite nanoparticles via microwave method: Investigation of photocatalytic performance of congo red degradation dye. Surf. Interfaces 25,. https://doi.org/10.1016/j.surfin.2021.101296 101296.

Mancuso, A., Sacco, O., Sannino, D., et al, 2020. Enhanced visible-light-driven photodegradation of Acid Orange 7 azo dye in aqueous solution using Fe-N co-doped TiO2. Arabian J. Chem. 13, 8347–8360. https://doi.org/10.1016/j.arabjc.2020.05.019.

Mohadesi, A., Ranjbar, M., 2016. Synthesis and characterization of TiO2 nanoparticles by microwave method and investigation its photovoltaic property. J. Mater. Sci.: Mater. Electron. 27, 862–866. https://doi.org/10.1007/s10854-015-3827-0.

Muthee, D.K., Dejene, B.F., 2021. Effect of annealing temperature on structural, optical, and photocatalytic properties of titanium dioxide nanoparticles. Heliyon. 7,. https://doi.org/10.1016/j.heliyon.2021.e07269 e07269.

Rajeswari, V.D., Eed, E.M., Elfasakhany, A., et al, 2021. Green synthesis of titanium dioxide nanoparticles using Laurus nobilis (bay leaf): antioxidant and antimicrobial activities. Applied Nanoscience. https://doi.org/10.1007/s13204-021-02065-2.

Rashid, M.M., Forte Tavčer, P., Tomšič, B., 2021. Influence of Titanium Dioxide Nanoparticles on Human Health and the Environment. Nanomaterials. 11, 2354.

Rathore, N., Kulshreshtha, A., Shukla, R.K., et al, 2020. Study on morphological, structural and dielectric properties of sol-gel derived TiO2 nanocrystals annealed at different temperatures. Physica B 582,. https://doi.org/10.1016/j.physb.2019.411969 411969.

Rebhi, A., Makhlouf, T., Njah, N., 2009. X-ray diffraction analysis of 99.1% recycled aluminium subjected to equal channel angular extrusion. Physics Procedia 2, 1263–1270.

Safiay, N.M., Abdul Rani, R., Ahmed Azhar, N.E., et al, 2021. Influence of Different Annealing Temperatures on the Structural and Optical Properties of TiO 2 Nanoparticles Synthesized via Sol-Gel Method: Potential Application as UV Sensor. Indonesian J. Chem. 21 (2), 2021 https://doi.org/10.22146/ijc.52255.

Sagadevan, S., Chowdhury, Z., Bin Johan, M., et al, 2018. Investigation on optical, dielectric and invitro anti-inflammatory responses of titanium dioxide (TiO 2) nanoparticles. Digest J. Nanomater. Biostruct. (DJNB) 13.

Santhi, K., Navaneethan, M., Harish, S., et al, 2020. Synthesis and characterization of TiO2 nanorods by hydrothermal method with different pH conditions and their photocatalytic activity. Appl. Surf. Sci. 500,. https://doi.org/10.1016/j.apsusc.2019.144058 144058.

Sharma, R., Sarkar, A., Jha, R., et al, 2020. Sol-gel–mediated synthesis of TiO2 nanocrystals: Structural, optical, and electrochemical properties. Int. J. Appl. Ceram. Technol. 17, 1400–1409. https://doi.org/https://doi.org/10.1111/ijac.13439.

Subagyo, R., Tehubijuluw, H., Utomo, W.P., et al, 2022. Converting red mud wastes into mesoporous ZSM-5 decorated with TiO2 as an eco-friendly and efficient adsorbent-photocatalyst for dyes removal. Arabian J. Chem. 15, 103754. https://doi.org/10.1016/j.arabjc.2022.103754.

Xie, G., Lu, W., Lu, D., 2015. Penetration of Titanium Dioxide Nanoparticles through Slightly Damaged Skin in Vitro and in vivo. J. Appl. Biomater. Funct. Mater. 13, 356–361. https://doi.org/10.5301/jabfm.5000243.

Zhang, J., Song, W., Guo, J., et al, 2012. Cytotoxicity of different sized TiO2 nanoparticles in mouse macrophages. Toxicol. Ind. Health 29, 523–533. https://doi.org/10.1177/0748233712442708.

Further reading

Horikoshi, S. and N. Serpone, Microwave Frequency Effects in Organic Synthesis. Microwaves in Organic Synthesis: 377-423.